Journal of Materials Chemistry A

ROYAL SOCIETY OF CHEMISTRY

PAPER

View Article Online
View Journal | View Issue



Cite this: *J. Mater. Chem. A*, 2020, **8**, 13585

# Investigation on the role of amines in the liquefaction and recrystallization process of $MAPbI_3$ perovskite†

Xi Yuan Feng,‡[ab] Kar Wei Ng,‡[ac] Shuang Peng Wang, *[ac] Wen Zhou Chen,[a] Zhen Zhong Zhang,[d] Wei Chen,[b] Yun Yang Zhao,[a] Bao Tu,[ab] Zi Kang Tang,[ac] Hui Pan *[ac] and Zhu Bing He *[b]

The amine-induced very fast liquefaction and recrystallization (L&R) process on organic–inorganic hybrid perovskites has been demonstrated to be an effective way to improve the quality of the as-deposited $MAPbI_3$ films and increase the feasibility of preparing large area perovskite solar cells (PSCs). Despite the effectiveness, the reaction mechanism of the L&R process is yet to be well understood. In this work, we investigate the fundamental influences of amines on the structural change of $MAPbI_3$ perovskite by studying the reaction between ammonia and a bulk $MAPbI_3$ crystal. By employing various techniques including *in situ* X-ray diffraction, Raman spectroscopy and Fourier transform infrared spectroscopy, we find that $NH_3$ effectively substitutes iodine in the perovskite crystal lattice, transforming the 3-dimensional (3D) lattice into a $MAPb(NH_3)_nI_3$ coordination complex-based system. The resulting coordination complex octahedral structures are only held together by weak forces of attraction, leading to the experimentally observed L&R process. First-principles calculations further confirm the feasibility of such L&R at room temperature. As a proof of concept, we demonstrated the use of liquefaction for substrate recycling of $MAPbI_3$ based solar cells with ammonia. Our results here provide deep insights for understanding the interaction mechanism, which can surely provide important guidance on improving the quality of perovskite films and related devices, as well as the recycling of toxic lead for long-term sustainability.

Received 13th April 2020
Accepted 20th June 2020

DOI: 10.1039/d0ta03995k

rsc.li/materials-a

## Introduction

Although the certified power conversion efficiency (PCE) of perovskite solar cells (PSCs) has recently reached 25.2% in lab scale devices,[1] the device stability and large-area fabrication are still critical issues for the commercialization of PSCs.[2] It is still challenging to obtain pinhole-free uniform perovskite thin films by using either solution-processed or vacuum-based deposition techniques.[3–7] Amines have been found to liquefy perovskite films (*e.g.* $CH_3NH_3PbI_3$ film)[8,9] and perovskite precursors (*e.g.* $PbI_2$ and $CH_3NH_3I$)[10–12] efficiently, while amine-treated perovskites can recrystallize into a conformal solid film upon the removal of amines. The liquefaction and recrystallization (L&R) process induced by amines enables precise control of the morphology and expands the possibility of preparing large area PSCs.[8–17] By applying the L&R process which lasts for only several seconds, it has been demonstrated that various amine gases, *e.g.* methylamine,[8] butylamine[18] and pyridine,[14] can effectively heal pinholes and the rough morphologies of $CH_3NH_3PbI_3$ (MPI) films, thus leading to respectable improvements in the process scalability, environmental stability, reduction of interfacial defect density, and hysteresis of MPI-based optoelectronic devices.[8,9,14,15,18–20]

Notably, the amine-induced L&R process has shown great promise in overcoming the bottleneck for the preparation of large-area perovskite solar cells. Chen *et al.* reported a new methylamine (MA) gas related deposition route for MPI films. A 36 $cm^2$ module exhibiting an efficiency up to 12.0% has been demonstrated using the L&R process alone, rather than the commonly used solvent or vacuum film forming techniques.[21] An advanced MA related dip-coating method has enabled the fabrication of large-scale MPI modules (12 $cm^2$ aperture area)

[a]*Joint Key Laboratory of the Ministry of Education, Institute of Applied Physics and Materials Engineering, University of Macau, Avenida da Universidade, Taipa, Macau 999078, China. E-mail: spwang@um.edu.mo; Tel: +853 8822 4048*

[b]*Department of Materials Science and Engineering, Shenzhen Key Laboratory of Full Spectral Solar Electricity Generation (FSSEG), Southern University of Science and Technology, No. 1088, Xueyuan Rd., Shenzhen, China. E-mail: hezb@sustech.edu.cn*

[c]*Department of Physics and Chemistry, Faculty of Science and Technology, University of Macau, Avenida da Universidade, Taipa, Macau 999078, China*

[d]*State Key Laboratory of Luminescence and Applications, Changchun Institute of Optics, Fine Mechanics and Physics, Chinese Academy of Sciences, No. 3888 Dongnanhu Road, Changchun 130033, China*

† Electronic supplementary information (ESI) available. See DOI: 10.1039/d0ta03995k

‡ These authors contributed equally to this work.

with an efficiency up to 16.0% and outstanding stability over 10 000 s under continuous output.[12] Jeong *et al.* developed a precursor solution obtained by liquefying an MPI crystal with MA gas. A high-quality MPI based solar cell was then prepared by scratch coating the precursor solution on a large area of 100 $cm^2$ and an average power conversion efficiency of 17.01% was achieved.[11]

Despite the usefulness of the L&R process, the actual working mechanism is still under debate and further exploration is urgently needed. One major challenge in understanding the reaction mechanism is that the reaction between amines and MPI is too fast for detection with conventional means.[15,22–24] This is particularly pronounced in common thin film solar cells in which the MPI film thickness is usually only hundreds of nanometres. Amines like $NH_3$ can easily penetrate through the crystal boundaries in the polycrystalline film and liquefy the crystal grains quickly. Indeed, Zhao *et al.*[22] first revealed the rapid bleaching of MPI film by $NH_3$ within a second, illustrating the quick reversible phase transformation of the perovskite film at sub-second response time. $CH_3NH_2$, another commonly used amine, has also been shown to be capable of healing rough and discontinuous MPI film within seconds.[8] The very short reaction time makes it difficult to probe the structural change during the intermediate steps. Another major challenge originates from the reaction complexity. In many cases, the final products and reaction kinetics have strong dependence on the type of amine involved as well as the reaction conditions. For example, Huang *et al.*[13] reported that $NH_3$ transforms MPI into $NH_4PbI_3$ through proton transfer from $CH_3NH_3^+$ to $NH_3$ in the compound.[14] This proton-transfer mechanism, however, is not readily observed in the reactions between MPI and other electron donating molecules (EDMs).[4] Even now, there is no consensus on the exact mechanism of how amines modify the structure of MPI.

In this paper, we explore the mechanism and chemical process of the L&R process in the reaction between MPI and $NH_3$, the simplest molecule in the amine family. Rather than the polycrystalline thin films commonly used in solar cells, millimeter-sized bulk MPI single crystals were utilized in this study to extend the reaction time to tens of minutes by pushing the reaction to the diffusion limited regime. The much longer total reaction time enables us to clearly observe the structural change of MPI during the process using *in situ* X-ray diffraction (XRD) and Raman spectroscopy. The results indicate that a high concentration of $NH_3$ facilitates the substitution of $I^-$ with $NH_3$ in the perovskite crystal lattice. This leads to the disintegration of the interconnected $PbI_6$ octahedral cages and transforms the continuous 3D lattice into weakly interacting $Pb(NH_3)_nI_{6-n}$ coordination complexes. Fourier transform infrared spectroscopy (FTIR) studies further confirm such substitution process by revealing the liberation of $CH_3NH_2^+$ and $I^-$ ions upon the breakdown of the lattice and these species subsequently interact with $NH_3$ to form $CH_3NH_2I$ and $NH_4I$. The coordination complex octahedra, the by-products, and the dissolved excess $NH_3$ are only held together by weak van der Waals forces, thus leading to the L&R of the MPI crystal. Our first-principles calculations demonstrate that the coordination process can reversibly occur spontaneously at room temperature, which agrees with the experimental findings and verifies the proposed model further. A flow chart can be found in the ESI† for a better understanding of our thoughts and organization of data. A proof-of-concept demonstration was carried out to show the potential application of the liquefaction process in the recycling of MPI based solar cells. Notably, the solar cells fabricated on the recycled conductive substrates and $NiO_x$ hole transport layers exhibit similar performance to the control devices, which clearly elucidates the viability of the liquefaction process in the simple yet effective substrate recycling scheme. An in-depth understanding of the reversible chemical and structural alterations resulting from the exposure to amines and other EDMs presented here can surely shed light on the development in the precursor preparation of amine–$MAPbI_3$ complexes in large-area PSCs, as well as the recycling of Pb for long-term sustainability.

## Results and discussion

Our investigation started with observing the change in appearance of an MPI crystal upon ammonia exposure. Bulk MPI crystals with millimeter-dimensions were used in our study, as shown in Fig. 1. The MPI crystal was placed in an ambient with continuous $NH_3$ supply at room temperature. Fig. 1a–f show the evolution of the reaction at different periods of time. After 5 minutes of $NH_3$ exposure, the originally dark MPI crystal (Fig. 1a) became slightly yellow in color (Fig. 1b). In addition, the edges between crystal facets became rounded and a noticeable swelling of the crystal can be seen. The increase in volume implies the incorporation of $NH_3$ into the crystal. As the exposure time increases, the crystal transformed completely into a yellowish liquid (Fig. 1c). Surprisingly, the yellow color faded upon further exposing the sample to $NH_3$, and the sample turned into a glittering and translucent "liquid" (Fig. 1d). The

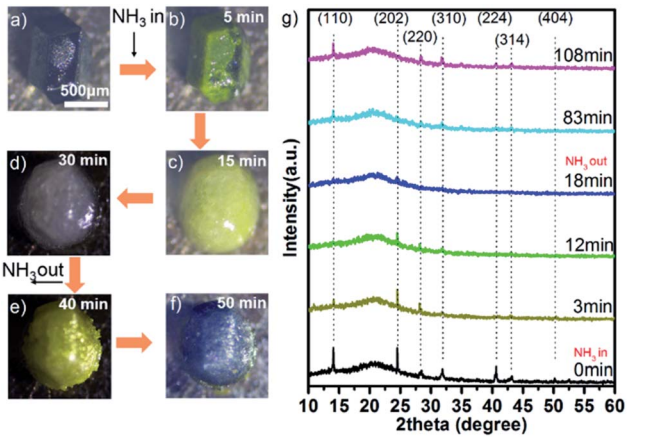


Fig. 1 *In situ* optical microscopy images (5× magnification) showing the L&R process of an MPI single crystal exposed to $NH_3$ (a–d) and the solidification process of the intermediate product when $NH_3$ is degassed (e and f). The scale bar is 500 μm. (g) Pseudo *in situ* XRD patterns showing the structural evolution of the MPI upon exposure to $NH_3$ and $NH_3$ degassing.

 

reaction complex was then flushed with $N_2$ to 'degas' the incorporated $NH_3$. The sample regained its yellowish color and dented edges after 10 minutes (Fig. 1e) and finally turned back into a greyish well-faceted oval-shaped solid (Fig. 1f). The evolution series here illustrate that the reaction is reversible and the sample can be recrystallized after the liquefaction induced by $NH_3$.

To confirm that the reaction is truly reversible, we employed pseudo *in situ* XRD to monitor the change in crystal structure during the process by using a homemade setup shown in Fig. S1.† $NH_3/N_2$ can be injected/removed through the soft-gel lid with a syringe to create a suitable ambient for the reaction. To obtain strong enough diffraction signals, multiple MPI crystals with random orientations were used in the *in situ* investigation. Fig. 1g reveals a series of $\omega-2\theta$ scans obtained at different times. The peaks at 14.08°, 24.48°, 28.48°, 31.86°, 40.64° and 43.24° can be indexed to the 110, 202, 220, 310, 224 and 314 diffractions of MPI crystals, respectively.[4,14,25–27] We can observe that these characteristic peaks disappear gradually with increasing exposure time in $NH_3$, indicating the gradual amorphization of the compound upon $NH_3$ incorporation. In addition to the vanishing XRD peaks, the originally black sample becomes yellow in color (see Fig. S3†), similar to what we observed in Fig. 1b. After around 30 minutes of $NH_3$ exposure, we cycle-purged the mini-compartment with $N_2$ to 'degas' $NH_3$ from the sample. A dramatic color change from yellow to black can be observed (Fig. S3†), signifying the conversion of the reaction complex back to crystalline MPI. The change in color agrees well with the $\omega-2\theta$ scans in Fig. 1g in which most of the characteristic perovskite peaks reappear after the $N_2$ purge. The peak at 14.08° shows a faster diminishing and recovery than the other peaks, which could be due to the anisotropic reaction. Notably, the 202 and 110 diffraction peaks cannot be fully recovered even after prolonged degassing of $NH_3$. Such observation may be attributed to the merging of the tiny crystal particles of different crystal orientations during the L&R process such that the crystals responsible for these two diffractions lose their original crystal orientations when recrystallizing from the liquid. Nevertheless, $NH_4PbI_3$ and $BA_2PbI_4$ (BA = butylamine), analogues of MPI, also display similar phenomena when exposed to $NH_3$ (see Fig. S5 and S6†). These observations clearly demonstrate the reversibility of the ammonia treatment, although the recrystallization process could lead to random orientations without proper control of the recrystallization conditions.

Although *in situ* XRD gives us direct proof for the L&R process, the actual reaction mechanism is still unclear. *In situ* Raman spectroscopy was therefore employed to study the structural change of the compounds during the process, using an environmental Raman stage standard accessory of our Raman spectrometer. Fig. 2a shows a series of normalized Raman spectra taken at different stages of the reversible reaction at room temperature. Two dominant peaks can be observed in all spectra in the series – one at 94 $cm^{-1}$ and the other one at or below 50 $cm^{-1}$. The former can be assigned to the stretching of Pb–I bonds while the vibrational modes below 50 $cm^{-1}$ are related to the bending of I–Pb–I bonds.[28] Fig. 2b shows the intensity variation of these two types of vibrations with reaction

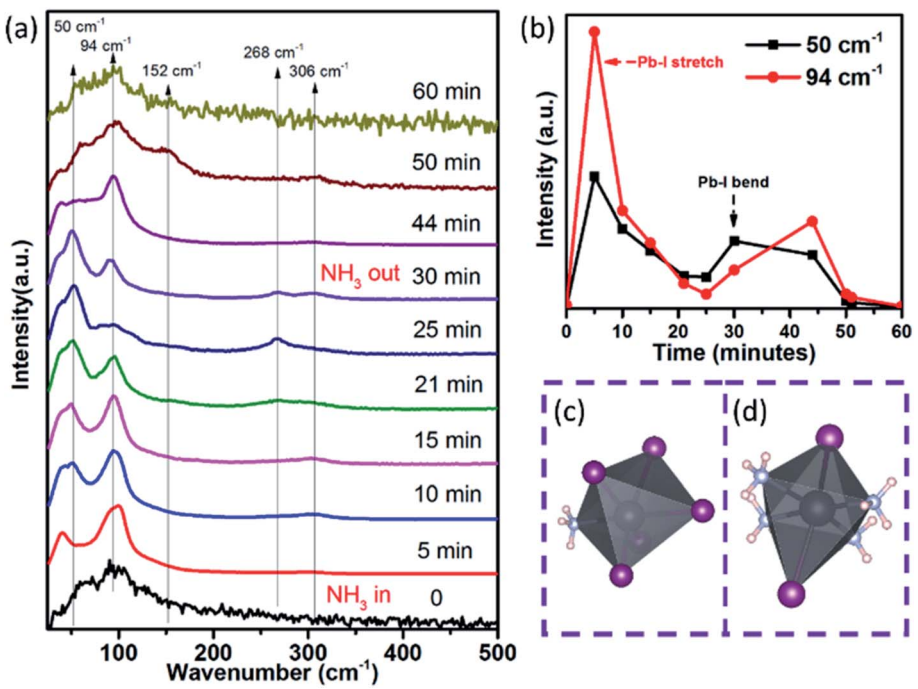


Fig. 2 (a) *In situ* Raman spectra of MPI upon $NH_3$ exposure and degassing. The variation of the Raman shifts describes the structural changes during the reversible reaction between MPI and $NH_3$. (b) Illustration of the peak intensity variation at 50 $cm^{-1}$ and 94 $cm^{-1}$. (c and d) Schematics of the $Pb(NH_3)_nI_{6-n}$ octahedron in the intermediate products of MPI when $NH_3$ gets incorporated into the lattice of MPI. The schematic shows how the substitution affects the symmetry of the octahedron.

time. When $NH_3$ was injected, the intensity of the two modes soared rapidly in the first 5 minutes and then reduced gradually with time. After 28 minutes, we purged the mini-compartment with $N_2$ to remove $NH_3$ from the atmosphere. The intensity of the two modes rose briefly and then eventually dropped back to a very low level similar to that of pristine perovskite. In addition, one can observe two weak Raman bands at around 268 $cm^{-1}$ and 306 $cm^{-1}$ which are related to the torsional modes of the $NH_2R$ group (*i.e.* $NH_3$ in this case) and Pb–N stretching, respectively.[29,30] These amine related vibrations clearly reveal the incorporation of $NH_3$ into the lattice, which accounts for the swelling of the MPI crystal displayed in Fig. 1a. These peaks only appeared upon $NH_3$ injection and vanished gradually during the $N_2$ purge. The evolution of the Raman spectra during the $NH_3$–$N_2$ cycle clearly shows the reversibility of the reaction, which is in line with our observations in appearance and XRD characterizations.

From the intensity variations of the characteristic Raman peaks, one can deduce the structural change during the reversible reaction. In the perovskite crystal lattice, each Pb-atom is bonded to 6 I-atoms, forming an octahedral cage structure with high symmetry. Such high crystal symmetry can result in silent Raman modes and weaken the overall Raman signal. Therefore, the two dominant Raman peaks corresponding to the bending and the stretching of the Pb–I bonds are very weak in pristine MPI. After 5 minutes of $NH_3$ exposure, the two Pb–I related bands rise dramatically, as seen in Fig. 2a and b. This is accompanied by the emergence of the Pb–N stretching mode at 268 $cm^{-1}$, which can be attributed to the formation of dative covalent bonds between $NH_3$ and Pb.[29] The implication of these observations is that $NH_3$ molecules, after getting incorporated into the MPI lattice, substitute I in the octahedral cage and transform the structure into a coordination complex.[22] This process, as illustrated in Fig. 2c, breaks the interconnections between adjacent octahedral cages and upsets the symmetry of the original perovskite lattice structure, thus leading to the surge in Raman signals. As the exposure time increases, however, these three characteristic Raman peaks weaken because the continuous supply of $NH_3$ facilitates the further replacement of Pb–I bonds with Pb–$NH_3$ dative bonds.[31] Although more $PbI_6$ octahedral cages are disconnected from their neighbors, each individual coordination complex octahedron becomes more symmetric upon increasing the number of coordinated $NH_3$ molecules (See Fig. 2d for an illustration). The gradual recovery of symmetry leads to a drop in scattering signal with exposure time. Interestingly, the $NH_2R$ (*i.e.* $NH_3$ in our case) related vibration at 268 $cm^{-1}$ does not appear until over 20 minutes of $NH_3$ exposure and it overtakes the Pb–N scattering mode afterwards, as seen in Fig. 2a. Such trend reveals that at the later stage of the reaction, most Pb-ions have already coordinated with a maximum number of $NH_3$ molecules and thus the subsequently incorporated $NH_3$ can only exist as molecules or $NH_4^+$ ions in the liquefied sample. The dissolution of excessive $NH_3$ at the end of the reaction is probably the reason for the fading of the yellow color in Fig. 1d. We note that the Pb–I bending and stretching bands always show up even after prolonged exposure of $NH_3$. This indicates that Pb–I bonds should still exist in the final coordination complex. As such, the most probable structure with the highest coordination number is $Pb(NH_3)_4I_2$, which exhibits the highest symmetry as well as charge neutrality. Indeed, our theoretical calculations do show that the formation of $Pb(NH_3)_4I_2$ is energetically favorable and this will be discussed in detail shortly. When $NH_3$ was removed from the reaction ambient at $t = 30$ min, the $NH_2R$ related peak reduced in intensity while the other three characteristic peaks grew stronger. This implies the vaporization of the dissolved $NH_3$ from the liquefied perovskite and the gradual conversion of the $Pb(NH_3)_nI_{6-n}$ coordination complex back to interlinked $PbI_6$ octahedral cages. Finally, after a prolonged $N_2$ purge, the sample solidified again and exhibited a weak Raman spectrum similar to that of the pristine MPI crystal, signifying the recovery of the highly symmetric perovskite crystal structure. The *in situ* Raman spectrum series here clearly demonstrate the reversible transformation between the $PbI_6$ octahedral cage based lattice structure and $Pb(NH_3)_nI_{6-n}$ coordination complex, which gives us great insight for understanding the mechanism of the L&R process.

Notably, our observation here is quite different from a previous model proposed by Huang *et al.*[13] who observed the reaction between MPI and $NH_3$ using pseudo *in situ* X-ray photoelectron spectroscopy. In their model, $NH_3$ displaces $CH_3NH_2$ in MPI to form $NH_4PbI_3$ in which the $PbI_6$ octahedral cages are well preserved. To verify this discrepancy, we synthesized $NH_4PbI_3$ powder and compared its Raman spectrum (see Fig. S2b†) with the spectra taken *in situ* in this work. Indeed, the characteristic bands at 99, 117 and 174 $cm^{-1}$ in $NH_4PbI_3$ are either very weak or absent in the Raman spectra in Fig. 2a. This indicates that $NH_4PbI_3$ is not formed during the reversible reaction in this work. The origin of such discrepancy can be attributed to the high concentration of $NH_3$ used in this work, which facilitates the formation of the $Pb(NH_3)_nI_{6-n}$ coordination complex rather than cation exchange at low $NH_3$ concentration.

The incorporated $NH_3$ interacts with not only Pb(II) ions, but also other species in the MPI crystal. FTIR measurement with an attenuated total reflectance accessory was conducted to study the interactions. Fig. 3 displays the FTIR spectra of pristine and liquefied MPI. We note that the feature peaks highlighted by the blue dotted line in the spectrum of pristine MPI are consistent with other previous studies.[32] Comparing the two spectra, one can observe the appearance of several new features in the liquefied sample. Among the additional peaks, the ones at 3245 and 3315 $cm^{-1}$ can be assigned to the symmetric and antisymmetric stretching modes of $NH_3$, which confirms the incorporation of $NH_3$ into the lattice. In addition, the symmetric $CH_3$ bending at 1388 $cm^{-1}$ as well as the symmetric and asymmetric $NH_3^+$ stretching at 3132 and 3179 $cm^{-1}$ stand out after $NH_3$ exposure. These can be attributed to the release of $CH_3NH_3^+$ from the perovskite motif during the disintegration of the interconnected $PbI_6$ octahedral cage structure.[29,32,33] The peak at 3012 $cm^{-1}$ belongs to the absorptions of $NH_4^+$, which gives a clue to the protonation of $NH_3$ *via* proton exchange between $CH_3NH_3^+$ and $NH_3$.[29] Such proton exchange process is also observed between $CH_3NH_3^+$ and other amines.[14] These

 

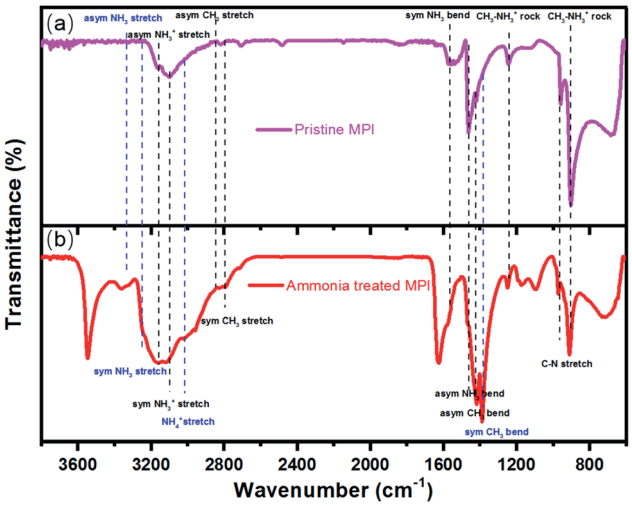


Fig. 3 FTIR spectra of (a) pristine MPI and (b) ammonia treated MPI. The differences between the two spectra illustrate the liberation of $CH_3NH_3^+$ in the $NH_3$ treatment process.

results not only confirm the liberation of $CH_3NH_3^+$ during the decomposition of the interconnected cage structure, but also demonstrate that proton exchange can occur between $NH_3$ and $CH_3NH_3^+$.

The formation of a coordination complex leads to the rupture of the interconnected cage structure and the liberation of the originally fixed $CH_3NH_3^+$ and $I^-$ ions. The latter may react with other cations, *e.g.* $CH_3NH_3^+$ or $NH_4^+$, to form new compounds or remain as mobile ions. However, these species are hard to detect due to their relatively weak vibrations in liquid form. Therefore, we solidified the reaction complex to obtain a relatively ordered structure for better Raman signals. By putting the perovskite crystal in an $NH_3$ ambient for over 48 hours, the reaction can reach an equilibrium such that the liquid can be coagulated into a yellowish solid, as illustrated in the inset of Fig. 4a. Raman spectroscopy was performed while the solid was still sealed inside the $NH_3$ atmosphere. Notably, its Raman spectrum in Fig. 4a shows great similarity with the spectra obtained from the liquefied MPI after 10 and 15 minutes of $NH_3$ exposure, *i.e.* the blue and pink curves in Fig. 2a. This implies that the yellowish solid should be in the early phase of the $NH_3$ coordination process. When the $NH_3$ concentration in the ambient increases, it takes a much longer time (over 96 hours) for the liquefied MPI to solidify and the final product becomes a white solid instead, as seen in the inset of Fig. 4b. From the resemblance between the Raman spectrum obtained from this white solid (see Fig. 4b) and that obtained from liquefied MPI after 25 minutes of exposure (the deep blue curve in Fig. 2a), one can deduce that the white solid is a product of the later reaction stage. We note that the characteristic Raman peaks are much sharper in the two solidified samples such that some weaker peaks, which are indistinguishable from the dominant peaks in Fig. 2a, can also be identified clearly. These new features include the bands at 66 and 121 $cm^{-1}$ (appears as a shoulder of the main peak at 108 $cm^{-1}$) in Fig. 4a and the

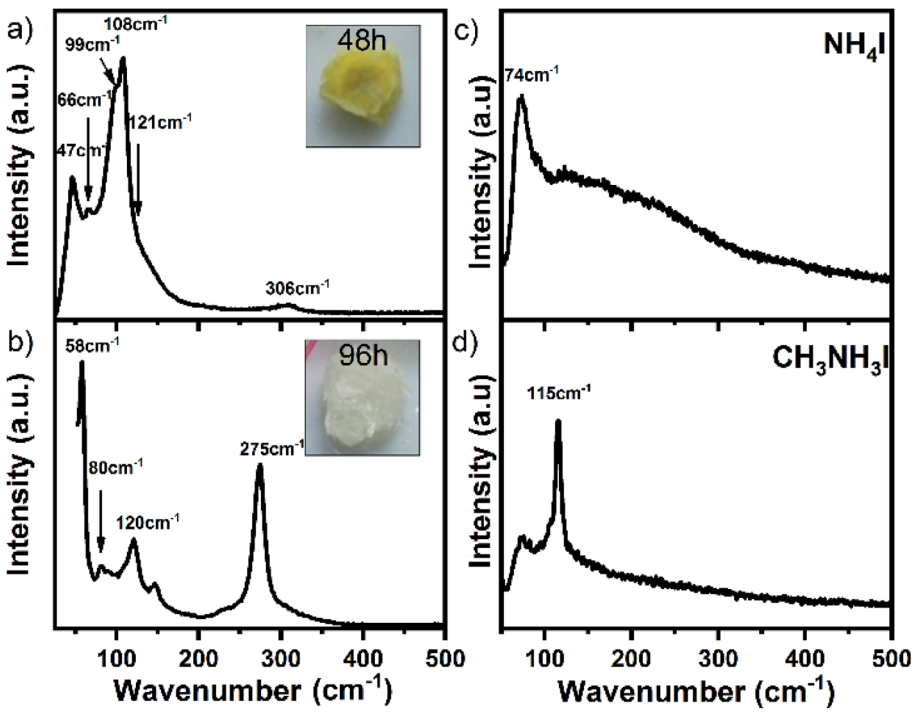


Fig. 4 (a) Raman spectrum of the solidified sample when MPI is placed in $NH_3$ for over 48 h (the inset is a photo of the sample). (b) Raman spectrum of the solidified sample when MPI is placed in $NH_3$ for over 96 h (the inset is a photo of the sample). (c) Raman spectrum of $NH_4I$ powder and (d) $CH_3NH_3I$ powder. The presence of $NH_4I$ and $CH_3NH_3I$ in the sample indicates the liberation of $I^-$ and $CH_3NH_3^+$ ions during the coordination process.

bands at 80 and 120 $cm^{-1}$ in Fig. 4b. To identify the origins of these new features, we measured the Raman spectra of commercially available $NH_4I$ and $CH_3NH_3I$, as illustrated in Fig. 4c and d, respectively. The bands at 66 $cm^{-1}$ in the yellow solid and 80 $cm^{-1}$ in the white solid can be attributed to $NH_4I$ while the one at around 120 $cm^{-1}$ in both solids should be related to $CH_3NH_3I$. The slight mismatches in peak wavenumbers are likely due to an error in resolving the weak peaks from the dominant ones, as well as the shift in vibrational resonances as a result of the interactions between $NH_4I$/$CH_3NH_3I$ and the surrounding $Pb(NH_3)_nI_{6-n}$ coordination complex. Nevertheless, the results here indicate the presence of $NH_4I$ and $CH_3NH_3I$ in the solidified samples and this confirms the liberation of $I^-$ and $CH_3NH_3^+$ ions during the coordination process.

Based on the observations described above, we believe that the reaction between MPI and $NH_3$ involves the substitution of I with $NH_3$ which leads to the transformation of the 3D interconnected $PbI_6$ octahedral lattice into a $Pb(NH_3)_nI_{6-n}$ coordination complex based structure. To validate the legitimacy of the proposed model, first-principles calculations were performed. Details of the structure models, simulation parameters and methods can be found in the ESI.† As discussed, MPI possesses a perovskite structure consisting of interconnected $PbI_6$ octahedral cages, which fix the $CH_3NH_3^+$ ions in place, as displayed schematically in Fig. 5a. Our calculations started with putting $NH_3$ molecules into the tetrahedral sites of the perovskite lattice unit cell and the structure was subsequently allowed to relax to the lowest energy state. Fig. 5b illustrates the fully relaxed structure with one $NH_3$ molecule incorporated into the $PbI_6$ octahedron. The structure clearly shows the substitution of I with $NH_3$ in each $PbI_6$ octahedral cage, which is in excellent agreement with our proposed model. Notably, the substitution process partially breaks the Pb–I–Pb interlinks among neighboring $PbI_6$ octahedral cages and the newly coordinated $NH_3$ only interacts very weakly with neighboring octahedra. Such weak interaction is evident from the very long calculated distance between neighboring I and H in adjacent $Pb(NH_3)I_5$ octahedra (see the ESI† for details). At high concentration of $NH_3$, the substitution can go further and the number of coordinated $NH_3$ molecules can increase from 1 to 4 (see Fig. 5b–e). Once the maximum coordination number, *i.e.* 4, is reached, any excess $NH_3$ can only exist as free molecules or $NH_4I$ in the structure, as observed in Fig. S14.† In the later stage of the reaction, most of the Pb–I–Pb interlinks would be replaced by weak van der Waals interactions among the coordinated $Pb(NH_3)_4I_2$ octahedra. These weak forces of attraction are unstable against thermal fluctuations, thus favoring the $Pb(NH_3)_nI_{6-n}$ complex structure to exist in liquid form at room temperature. In addition, the calculated structures in Fig. 5b–e also confirm the liberation of $I^-$ and $CH_3NH_3^+$ ions as a result of the disintegration of the 3D lattice. These species may exist as ions or interact with $NH_3$ to form $CH_3NH_2$, $CH_3NH_3I$ and $NH_4I$. Notably, these molecules are quite uniformly spread out in the entire structure and are held together with the coordination complex octahedra by weak van der Waals forces. An implication of this model is that neither $NH_4I$ nor $CH_3NH_3I$ will be able to form a complete crystal structure by themselves even when the complex structure is solidified. This can be verified by comparing the XRD spectrum of the white solidified sample with those of $NH_4I$ and $CH_3NH_3I$. As shown in Fig. S4,† the three spectra are completely different from one another, confirming that the solidified sample does not contain the conventional phases of $NH_4I$ and $CH_3NH_3I$. Therefore, we believe that the $NH_4I$ and $CH_3NH_3I$ molecules are uniformly distributed in the lattice formed by $Pb(NH_3)_nI_{6-n}$, which facilitates the recrystallization of the MPI perovskite structure upon removal of $NH_3$.

Based on the mechanism described above, we evaluate the reaction feasibility by estimating the formation energies of the coordination complexes. Table S3† displays the formation energies of $MAPb(NH_3)_nI_{6-n}$, with $n$ varying from 1 to 5. The formation energies of all the MPI-$n(NH_3)$ systems are positive with values ranging from 0.284 to 0.358 eV per $NH_3$, which means that the formation processes are endothermic. Despite the endothermic nature of the reaction, our calculated formation energies, varying between 0.071 and 0.090 eV per atom, are still well below the criterion of 0.1 eV per atom, which is the exfoliation energy that has been established from the analysis of

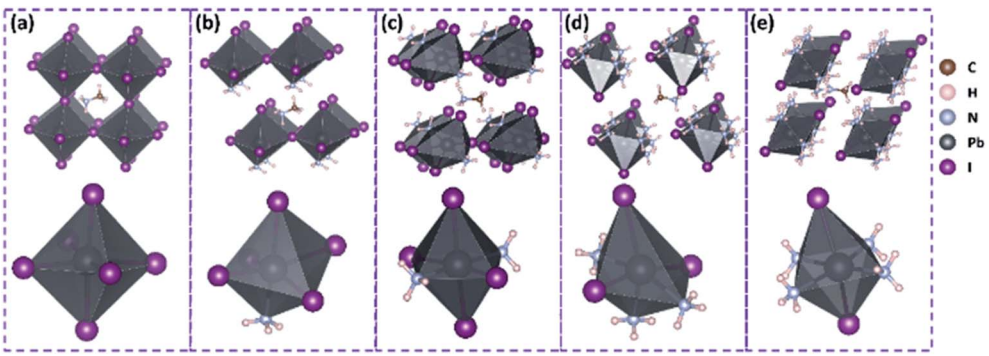


Fig. 5 Schematic diagrams illustrating the structural evolution process of MPI in an $NH_3$ ambient based on first principles calculations. (a) The structure of pristine MPI, and (b–e) the fully relaxed structure with one (b), two (c), three (d) and four (e) $NH_3$ molecules incorporated into the $PbI_6$ octahedron, respectively. The 2 × 2 × 2 matrix schematics describe the spatial relationship and the bond connection between the adjacent octahedral cages. The lattice structure is disintegrated gradually when $NH_3$ molecules come into the lattice and interact with the lead atom. The single octahedral schematics show how the $NH_3$ molecules come into the octahedral cages and gradually replace I.

 

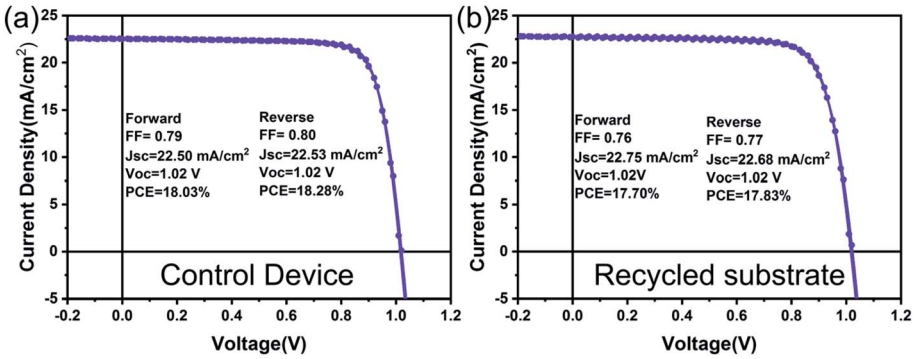


Fig. 6 *I–V* curves of (a) the control device with a PCE of 18.28% and (b) a device based on the recycled substrate with a PCE of 17.83%.

thousands of solids for the formation of stable 2D layers.[34] The extremely low formation energies signify the easy formation of the $CH_3NH_3PbI_3$-$n(NH_3)$ systems. Small values of formation energies for the $CH_3NH_3PbI_3$-$n(NH_3)$ systems also imply the reversibility of the reactions. The theoretical results exhibit excellent agreement with our experimental results and this unambiguously validates our proposed reaction mechanism that involves the reversible transformation of the rigid 3D perovskite lattice into weakly attracting coordination complex systems.

Notably, the L&R investigated here is highly selective to organic–inorganic hybrid perovskites. This implies that we can potentially use amines to extract and isolate the active layer from other functional layers and substrate in a full solar cell structure, thus paving the way towards the recycling of Pb-containing perovskites as well as the expensive ITO or FTO based conductive substrates with the functional layers attached. As a preliminary attempt, we applied the liquefaction process on an MPI solar cell with a structure of ITO/$NiO_x$/MPI/PCBM/BCP/Ag. The MPI layer remains well attached to other functional layers even after being liquefied by $NH_3$. Therefore, to increase the fluidity, ammonia solutions are used in the demonstration, so the active layer can be readily dissolved such that the $NiO_x$ coated ITO substrate can be easily recovered from the device. The same solar cell structures were then fabricated on the recovered substrates. Fig. 6 shows the photovoltaic characteristics of the devices fabricated on fresh and recycled substrates. The PCE of the control device is at 18.28% (Fig. 6a), which drops slightly to 17.83% in the MPI solar cell re-constructed on the recycled ITO/$NiO_x$ substrate (Fig. 6b). The role of water in the recycling process can be seen directly in Fig. S7c and d.† Although water is well known for its capability in decomposing MPI, the MPI layer cannot be well dissolved and the substrate cannot be extracted even when the device is dipped into water for a prolonged period of time. In sharp contrast, the dissolution of MPI happens immediately in aqueous ammonia, and a clear substrate can be obtained in 20 min. To further show that ammonia is the active ingredient for the substrate recovery process, isopropanol was used instead of water as the solvent. Similar recycling proficiency was achieved in terms of solar cell performances (Fig. S7 and Table S1†). Some other amines or their solutions, *e.g.* methylamine (MA)/ethanol, ethylamine (EA)/ethanol and butylamine (BA) were also used for the demonstration of the amine-assisted recycling. Details about the partially recycled device performance parameters can be found in the ESI (Fig. S7 and Table S1†). The preliminary results here demonstrate a simple yet efficient method of recycling the expensive ITO substrate without organic solvents with high boiling points, which would be an important first step in the complete and low-cost recycling of perovskite based solar cells for long-term sustainability.[35]

## Conclusions

In summary, we investigated the L&R process of MPI in an $NH_3$ ambient. With the use of *in situ* XRD, Raman spectroscopy and FTIR, we observed that at a high concentration of $NH_3$, MPI underwent a significant structural change which involved the substitution of I with $NH_3$ in the perovskite crystal lattice. Such substitution transforms the original 3D crystal into an $MAPb(NH_3)_nI_3$ coordination complex in which the $Pb(NH_3)_nI_{6-n}$ octahedral structures are only held together by weak van der Waals forces of attraction, thus resulting in the observed L&R process. The feasibility of this reaction mechanism is further validated by first-principles calculations. A preliminary demonstration showed the potential application of ammonia in recycling MPI based solar cells. The performance of the devices with recycled device parts is almost identical to that of the control devices. This unprecedented understanding paves the pathway towards the development in the precursor preparation of amine–$MAPbI_3$ complexes in large-area PSCs, as well as the recycling of Pb in MPI for long-term sustainability.

## Experimental section

### Materials

$CH_3NH_3I$ (MAI), $CH_3CH_2CH_2CH_2NH_3I$ (BAI) and $PbI_2$ were purchased from Xi'an Polymer Light Technology Corporation and were used without further processing. $NH_4I$ was purchased from Shanghai Aladdin Bio-Chem Technology Co., Ltd. $Ni(NO_3)_2 \cdot 6H_2O$ was purchased from Alfa. MPI single crystals were grown in solution *via* the temperature-lowering (TL) method as described in our previous work.[26]

### Characterization

The XRD measurements were carried out in a Rigaku Smart Lab system (Japan). Raman spectra were recorded using a confocal laser Raman spectrometer (Lab RAM HR Evolution, Horiba, Japan) with a 473 nm solid-state laser as the excitation source. FTIR spectra were measured using a VERTEX 70 FTIR spectrometer (Bruker, Germany) with an ATR accessory.

### Theoretical calculations

First-principles calculations were performed within the Vienna *Ab initio* Simulation Package (VASP),[36] based on Density Functional Theory (DFT). The projector augmented wave (PAW) method[37] was employed to describe the interactions between the ionic cores and valence electrons, with the valence electrons employed being $6s^2 6p^2$, $5s^2 5p^5$, $2s^2 2p^3$, $2s^2 2p^2$, and $1s^1$ for Pb, I, N, C, and H, respectively. The correlation and exchange interactions were described by the generalized gradient approximation (GGA) parametrization of Perdew–Burke–Ernzerhof (PBE) functionals.[38]

More experimental details, *e.g. in situ* measurement setups, fabrication and performance of the perovskite solar cell and theoretical calculations, can be found in the ESI.†

## Conflicts of interest

The authors declare no competing financial interest.

## Acknowledgements

The authors thank Dr S. X. Hu (Materials Characterization and Preparation Center), Mr H. Q. Yi MSE of SUSTech and Dr Y. Yang of IAPME of UM for help with the characterization involved in this work. This work was funded by the Science and Technology Development Fund, Macau SAR (file no. 199/2017/A3, 0038/2019/A1, 0125/2018/A3, 084/2016/A2, 051/2017/A, 0102/2019/A2, and 0035/2019/AGJ) and Multi-Year Research Grants (MYRG2017-00149-FST, MYRG2017-00152-FST, SRG2016-00085-FST, SRG2016-00073-FST, MYRG2017-00027-FST, and MYRG2018-00003-IAPME) from the University of Macau. Z. B. He acknowledges the National Natural Science Foundation of China (No. 61775091), the Shenzhen Key Laboratory Project (No. ZDSYS201602261933302) and the Natural Science Foundation of Shenzhen Innovation Committee (No. JCYJ20180504165851864).

## References

1 www.nrel.gov/pv/assets/pdfs/best-research-cell-efficiencies.20200311.pdf, NREL, 2020.
2 Y. Rong, Y. Hu, A. Mei, H. Tan, M. I. Saidaminov, S. I. Seok, M. D. McGehee, E. H. Sargent and H. Han, *Science*, 2018, **361**, eaat8235.
3 W. Chen, Y. C. Zhou, L. J. Wang, Y. H. Wu, B. Tu, B. B. Yu, F. Z. Liu, H. W. Tam, G. Wang, A. B. Djurisic, L. Huang and Z. B. He, *Adv. Mater.*, 2018, **30**, 1800515.
4 W. Chen, L. M. Xu, X. Y. Feng, J. S. Jie and Z. B. He, *Adv. Mater.*, 2017, **29**, 1603923.
5 Y. Deng, X. Zheng, Y. Bai, Q. Wang, J. Zhao and J. Huang, *Nat. Energy*, 2018, **3**, 560–566.
6 Z. Li, T. R. Klein, D. H. Kim, M. Yang, J. J. Berry, M. F. A. M. van Hest and K. Zhu, *Nat. Rev. Mater.*, 2018, **3**, 18017.
7 Y. Wu, W. Chen, Y. Lin, B. Tu, X. Lan, Z. Wu, R. Liu, A. B. Djurišić and Z. B. He, *ACS Appl. Energy Mater.*, 2018, **1**, 3984–3991.
8 Z. Zhou, Z. Wang, Y. Zhou, S. Pang, D. Wang, H. Xu, Z. Liu, N. P. Padture and G. Cui, *Angew. Chem., Int. Ed.*, 2015, **54**, 9705–9709.
9 Y. Zong, Y. Zhou, M. Ju, H. F. Garces, A. R. Krause, F. Ji, G. Cui, X. C. Zeng, N. P. Padture and S. Pang, *Angew. Chem., Int. Ed.*, 2016, **55**, 14723–14727.
10 H. Chen, F. Ye, W. Tang, J. He, M. Yin, Y. Wang, F. Xie, E. Bi, X. Yang, M. Gratzel and L. Han, *Nature*, 2017, **550**, 92–95.
11 D.-N. Jeong, D.-K. Lee, S. Seo, S. Y. Lim, Y. Zhang, H. Shin, H. Cheong and N.-G. Park, *ACS Energy Lett.*, 2019, **4**, 1189–1195.
12 X. Huang, R. Chen, G. Deng, F. Han, P. Ruan, F. Cheng, J. Yin, B. Wu and N. Zheng, *J. Am. Chem. Soc.*, 2020, **142**, 6149–6157.
13 W. Huang, J. S. Manser, S. Sadhu, P. V. Kamat and S. Ptasinska, *J. Phys. Chem. Lett.*, 2016, **7**, 5068–5073.
14 S. M. Jain, Z. Qiu, L. Haggman, M. Mirmohades, M. B. Johansson, T. Edvinsson and G. Boschloo, *Energy Environ. Sci.*, 2016, **9**, 3770–3782.
15 S. R. Raga, L. K. Ono and Y. Qi, *J. Mater. Chem. A*, 2016, **4**, 2494–2500.
16 Z. Zhou, S. Pang, F. Ji, B. Zhang and G. Cui, *Chem. Commun.*, 2016, **52**, 3828–3831.
17 S. Lee, J. H. Park, B. R. Lee, E. D. Jung, J. C. Yu, D. Di Nuzzo, R. H. Friend and M. H. Song, *J. Phys. Chem. Lett.*, 2017, **8**, 1784–1792.
18 Z. Liu, K. Meng, X. Wang, Z. Qiao, Q. Xu, S. Li, L. Cheng, Z. Li and G. Chen, *Nano Lett.*, 2020, **20**, 1296–1304.
19 L. Zuo, S. Dong, N. De Marco, Y.-T. Hsieh, S.-H. Bae, P. Sun and Y. Yang, *J. Am. Chem. Soc.*, 2016, **138**, 15710–15716.
20 X. Yu, H. Yan and Q. Peng, *J. Phys. Chem. A*, 2017, **121**, 6755–6765.
21 H. Chen, F. Ye, W. Tang, J. He, M. Yin, Y. Wang, F. Xie, E. Bi, X. Yang, M. Grätzel and L. Han, *Nature*, 2017, **550**, 92–95.
22 Y. Zhao and K. Zhu, *Chem. Commun.*, 2014, **50**, 1605–1607.
23 C. Bao, J. Yang, W. Zhu, X. Zhou, H. Gao, F. Li, G. Fu, T. Yu and Z. Zou, *Chem. Commun.*, 2015, **51**, 15426–15429.
24 L. Zhu, Y. Xu, P. Zhang, J. Shi, Y. Zhao, H. Zhang, J. Wu, Y. Luo, D. Li and Q. Meng, *J. Mater. Chem. A*, 2017, **5**, 20874–20881.
25 Y. Y. Dang, Y. Liu, Y. X. Sun, D. S. Yuan, X. L. Liu, W. Q. Lu, G. F. Liu, H. B. Xia and X. T. Tao, *CrystEngComm*, 2015, **17**, 665–670.
26 X. Feng, H. Su, Y. Wu, H. Wu, J. Xie, X. Liu, J. Fan, J. Dai and Z. He, *J. Mater. Chem. A*, 2017, **5**, 12048–12053.
27 Y. H. Wu, W. Chen, G. Chen, L. Y. Liu, Z. B. He and R. C. Liu, *Nanomaterials*, 2018, **8**, 356.

 

28 C. Quarti, G. Grancini, E. Mosconi, P. Bruno, J. M. Ball, M. M. Lee, H. J. Snaith, A. Petrozza and F. D. Angelis, *J. Phys. Chem. Lett.*, 2014, **5**, 279–284.
29 R. F. Warren and W. Y. Liang, *J. Phys.: Condens. Matter*, 1993, **5**, 6407–6418.
30 M. Baibarac, I. Baltog and S. Lefrant, *J. Solid State Chem.*, 2009, **182**, 827–835.
31 L. C. Yuhallada and A. H. Francis, *J. Phys. Chem.*, 1990, **94**, 7518–7523.
32 T. Glaser, C. Müller, M. Sendner, C. Krekeler, O. E. Semonin, T. D. Hull, O. Yaffe, J. S. Owen, W. Kowalsky, A. Pucci and R. Lovrinčić, *J. Phys. Chem. Lett.*, 2015, **6**, 2913–2918.
33 G. I. Gurina and K. V. Savchenko, *J. Photochem. Photobiol., A*, 1995, **86**, 81–84.
34 M. Ashton, J. Paul, S. B. Sinnott and R. G. Hennig, *Phys. Rev. Lett.*, 2017, **118**, 106101–106106.
35 A. Binek, M. L. Petrus, N. Huber, H. Bristow, Y. Hu, T. Bein and P. Docampo, *ACS Appl. Mater. Interfaces*, 2016, **8**, 12881–12886.
36 G. Kresse and J. Furthmüller, *Phys. Rev. B*, 1996, **54**, 11169.
37 P. E. Blöchl, *Phys. Rev. B: Condens. Matter Mater. Phys.*, 1994, **50**, 17953.
38 J. P. Perdew, K. Burke and M. Ernzerhof, *Phys. Rev. Lett.*, 1996, **77**, 3865.